Diagnosing surfzone impacts on inner-shelf flow spatial variability using realistic model experiments with and without surface gravity waves

Xiaodong Wu[1], Falk Feddersen[1], and Sarah N. Giddings[1]

[1]*Scripps Institution of Oceanography, La Jolla, California, USA*

Submitted to *Journal of Physical Oceanography,*

January 15, 2021

Corresponding author address:
X. Wu, Scripps Institution of Oceanography, University of California, San Diego, 9500 Gilman Dr., La Jolla CA 92093-0209
E-mail:x1wu@ucsd.edu

ABSTRACT

Rip currents are generated by surfzone wave breaking and are ejected offshore inducing inner-shelf flow spatial variability (eddies). However, surfzone effects on the inner-shelf flow spatial variability have not been studied in realistic models that include both shelf and surfzone processes. Here, these effects are diagnosed with two nearly identical twin realistic simulations of the San Diego Bight over summer to fall where one simulation includes surface gravity waves (WW) and another that does not (NW). The simulations include tides, weak to moderate winds, internal waves, submesoscale processes, and have surfzone width $L_{\rm sz}$ of $96(\pm 41)$ m (≈ 1 m significant wave height). Flow spatial variability metrics, alongshore root mean square vorticity, divergence, and eddy cross-shore velocity, are analyzed in a $L_{\rm sz}$ normalized cross-shore coordinate. At the surface, the metrics are consistently ($> 70\%$) elevated in the WW run relative to NW out to $5L_{\rm sz}$ offshore. At $4L_{\rm sz}$ offshore, WW metrics are enhanced over the entire water column. In a fixed coordinate appropriate for eddy transport, the eddy cross-shore velocity squared correlation between WW and NW runs is < 0.5 out to 1.2 km offshore or 12 time-averaged $L_{\rm sz}$. The results indicate that the eddy tracer (*e.g.,* larvae) transport and dispersion across the inner-shelf will be significantly different in the WW and NW runs. The WW model neglects specific surfzone vorticity generation mechanisms. Thus, these inner-shelf impacts are likely underestimated. In other regions with larger waves, impacts will extend farther offshore.

1. Introduction

The coastal ocean is a conduit for the material (*e.g.,* larvae, nutrients and pollutants) exchange between the coastline and the open ocean (*e.g.,* Brink 2016) and is comprised of dynamically different sub-regions including, from the shoreline to offshore, the surf zone, inner-shelf to mid-shelf, and outer-shelf. The surf zone (surfzone) extends a width of L_{sz} from the shoreline to the wave breakpoint location and is strongly forced by surface gravity waves (*e.g.,* Battjes 1988). The inner-shelf is seaward of the surfzone and typically extends to ≈ 15 m water depth and transitions to the mid-shelf. Within the inner-shelf, both alongshore (*e.g.,* Lentz 2001; Lentz and Fewings 2012) and cross-shore (Fewings et al. 2008) winds are important in driving currents. Bathymetric irregularities steer the flow (*e.g.,* Largier 2020), favoring the generation of coastal eddies (*e.g.,* Kirincich 2016). Submesoscale density fronts frequently develop in the inner- and mid-shelf (Dauhajre et al. 2017; Wu et al. 2021). Inner-shelf cross-shore transport can be driven by nonlinear internal waves (*e.g.,* Grimes et al. 2019; Davis et al. 2020) and diurnal heating and cooling (*e.g.,* Monismith et al. 2006). Both wind-driven Ekman and submesoscale flows are important to offshore transport of shoreline released tracer through the mid-shelf (Wu et al. 2020). In addition, the surface gravity wave associated Stokes drift induces Stokes-Coriolis forces resulting in compensating Eulerian offshore-directed undertow (Lentz et al. 2008; Kirincich et al. 2009).

Within the surfzone, wave breaking generates turbulence (Feddersen 2012), vertically mixing the water column (Hally-Rosendahl et al. 2014), and, for obliquely incident waves, drives surfzone alongshore currents (Longuet-Higgins 1970; Feddersen et al. 1998). Surfzone vorticity is generated by finite-crest wave breaking (Peregrine 1998; Feddersen 2014), wave groups (*e.g.,* Reniers et al. 2004; Long and Özkan-Haller 2009), or irregular bathymetry (*e.g.,* Haller et al. 2002; Castelle and Coco 2013) which eventually leads to transient (TRC, Johnson and Pattiaratchi 2006; Spydell and Feddersen 2009) or bathymetrically controlled (BRC, Dalrymple et al. 2011; Moulton et al. 2017) rip currents. Rip currents (TRCs and BRCs) export material $\sim 2L_{\mathrm{sz}}$ to $\sim 4L_{\mathrm{sz}}$ onto the inner-shelf both in observations (MacMahan et al. 2010; Hally-Rosendahl et al. 2014; Brown et al. 2015; Hally-Rosendahl et al. 2015) and models (Reniers et al. 2009; Suanda and Feddersen 2015) resulting in inner-shelf eddies (flow spatial variability). Rip currents strengthen with increasing wave height or equivalently surfzone width L_{sz} (*e.g.,* Haller et al. 2002; Suanda and Feddersen 2015; Moulton et al. 2017). BRC strength also depend on bathymetric variability (*e.g.,* Reniers et al. 2007; Castelle et al. 2014; Uchiyama et al. 2017) and the offshore extent of BRCs is reduced for stronger inner-shelf alongshelf flow (Winter et al. 2014). The cross-shore extent of BRC inner-shelf eddies is modulated by surfzone and inner-shelf temperature differences in observations and models (Moulton et al. 2020). However, none of the cited modeling studies included realistic shelf processes such as winds, barotropic or baroclinic tides, or other inner-shelf processes.

Rip currents have secondary effects on the stratified inner-shelf induced by strong TRC mixing on the inner-shelf within $2L_{\mathrm{sz}}$ to $4L_{\mathrm{sz}}$ of the shoreline which have also only been studied in a few idealized models. TRC induced vertical mixing on a stratified shelf induces a cross-shore circulation cell (Kumar and Feddersen 2017b), driving cross-shelf subsurface tracer transport $\sim 10L_{\text{sz}}$ offshore (Kumar and Feddersen 2017c). This circulation cell is self-similar and can be scaled by the stratification and the rip current cross-shore eddy kinetic energy flux (Grimes and Feddersen 2020). This TRC induced exchange across the inner-shelf exchange dominates over the thermally driven exchange for typical Southern California conditions (Grimes et al. 2020). These idealized modeling studies also did not consider wind, barotropic or baroclinic tidal forcing, or other important inner-shelf processes.

Idealized modeling studies of canonical inner-shelf processes (*e.g.,* winds and tides) have not considered surfzone effects (*e.g.,* Austin and Lentz 2002; Castelao et al. 2010; Horwitz and Lentz 2014). Furthermore, most realistic inner-shelf modeling studies do not include surfzone effects (*e.g.,* Ganju et al. 2011; Romero et al. 2013; Dauhajre et al. 2017; Suanda et al. 2018; Dauhajre et al. 2019), with a few exceptions. The few realistic inner-shelf modeling studies which do include surfzone effects (Kumar et al. 2015, 2016; Wu et al. 2020, 2021) have not examined surfzone effects on inner-shelf flow spatial variability. The range and complexity of inner-shelf processes (*e.g.,* winds, barotropic tides, alongshore pressure gradients, internal waves, diurnal heating/cooling, bathymetric steering, submesoscale flows, and local Stokes drift induced flows) make it challenging to separate out surfzone effects on inner-shelf flow spatial variability in realistic models as well as in observations. Identical twin realistic simulations where one simulation has waves and surfzone effects and another without waves are required to diagnose surfzone effects on the inner-shelf.

Here, we investigate the surfzone effects on inner-shelf flow spatial variability using two nearly identical realistic twin simulations spanning from the outer-shelf to the shoreline using realistic bathymetry, oceanic, and atmospheric forcing. One simulation includes surface gravity waves (denoted with-waves, WW) and thus a surfzone (Wu et al. 2020), whereas another does not include waves (no-waves, NW). Analysis focuses on a 3-month (midsummer to fall) period characterized by weak to moderate winds, weak to moderate surface wave forcing, diurnal heating and cooling, active internal waves, and submesoscale frontal processes (Wu et al. 2020). Surfzone effects on the inner shelf are examined by comparing metrics related to flow spatial variability between the WW and NW runs. Model configuration, regional oceanographic conditions and analysis methods are provided in Section 2. Comparisons between the WW and NW runs using the flow spatial variability metrics are presented in Section 3. The role of inner-shelf processes in modulating surfzone effects on inner-shelf flow spatial variability, the effect of neglected surfzone vorticity generation mechanisms, and the inner-shelf effects in other regions are discussed in Section 4. Section 5 is a summary.

2. Method

FIG. 1

FIG. 2

a. Model configuration

The with-waves (WW) and no-waves (NW) runs use the Coupled Ocean-Atmosphere-Wave-Sediment-Transport (COAWST) model system (Warner et al. 2010; Kumar et al. 2012) with the three-dimensional, hydrostatic Regional Ocean Modeling System (ROMS) circulation model (Shchepetkin and McWilliams 2005) and the Simulating Waves Nearshore model (SWAN) (Booij et al. 1999). The NW run is not coupled to SWAN and thus has no surface gravity waves. Wu et al. (2020) provides a full description of model configuration. The model grid ($15 \times 36\,\mathrm{km}^2$) spans from Punta Bandera (PB), Mexico to the Tijuana River Estuary (TJRE) and the San Diego Bay, US (Fig. 1a). The horizontal grid resolution varies from 110 m at the three open boundaries down to 8 m near the TJRE. NOAA 1/3-arc-second coastal digital elevation is used for bathymetry with depth h spanning 70 m to -2 m (Fig. 1a) with wetting/drying enabled. The local Coriolis parameter is $f = 7.8\times10^{-5}\,\mathrm{s}^{-1}$. The vertical ($z$) stretched grid has 15 $s-$levels with enhanced surface and bottom resolution. NOAA/NAM surface fluxes (winds, heat and precipitation) are used. Vertical mixing uses a $k-\epsilon$ scheme and the horizontal eddy viscosity is constant at $0.5\,\mathrm{m}^2\,\mathrm{s}^{-1}$. ROMS inherits realistic oceanic forcing from three one-way nested parent runs downscaled from the California Current System to the Southern California Bight allowing remotely generated internal tides, shelf waves, and eddies to enter the domain (Wu et al. 2020). SWAN boundary conditions are provided by CDIP wave model frequency-directional wave spectra (O'Reilly et al. 2016). SWAN uses random wave dissipation of Battjes and Stive (1985) with breaking parameter $\gamma = 0.5$. Note, SWAN is a wave averaged model and thus the WW run does not include finite-crest wave breaking or wave group vorticity generation mechanisms (Feddersen 2014). The grid receives small and realistic freshwater inputs at PB at constant $Q_r = 1.53\,\mathrm{m}^3\,\mathrm{s}^{-1}$ and TJRE following intermittent rainfall events (Fig. 1a). Analysis is performed with hourly model output over the summer to fall transition (22 July to 18 October 2015, denoted the *analysis period*) and within a $2 \times 4\,\mathrm{km}^2$ *nearshore study region* (red rectangle in Fig. 1a) that has a roughly straight shoreline and is located $5.2\,\mathrm{km}$ north of PB and $3.0\,\mathrm{km}$ south of the TJRE mouth. The nearshore study region's southern boundary is $7.8\,\mathrm{km}$ from the grid southern boundary. The nearshore study region has a mean resolution of $(18, 26)\,\mathrm{m}$ in the cross- (x, positive onshore) and alongshore (y, positive northward) directions, where $x = 0\,\mathrm{m}$ corresponds to where time- and alongshore (within nearshore study region) average total water depth is zero. The vertical coordinate is represented by z and t is time. The bottom slope is approximately 0.04 onshore of $h = 1$ m, 0.015 from $h = 1$ m to $h = 10$ m, and farther offshore is ≈ 0.007 (Fig. 2). Cross-shore and alongshore velocity components are denoted (u, v), respectively.

b. Regional oceanographic conditions

On the shelf, the model solutions include realistic wind-driven, barotropic tidal, internal tides, alongshelf pressure gradient driven flows, and submesoscale motions (Wu et al. 2020). The barotropic tides have peak amplitude ≈ 1 m. Conditions at shelf site S (22 m depth, Figs. 1a,2a1) indicate the range of variability in the model forcing and response. Winds are largely southeastward directed with intermittent northward events at low ($< 5\,\mathrm{m\,s^{-1}}$) to moderate ($5 - 8\,\mathrm{m\,s^{-1}}$) speeds (Fig. 1b). The significant wave height H_s varies between 0.5 to 1.45 m (Fig. 1c), with typically southerly incident waves that drive northward alongshore surfzone currents (Wu et al. 2020). The site S alongshelf depth-averaged current V_{S} varies $\pm 0.2\ \mathrm{m\,s^{-1}}$ largely subtidally driven by alongshelf pressure gradients, but also with tidal variability (Fig. 1d). The site S top-to-bottom buoyancy frequency $N^2 = -(g/\rho_0)\Delta\rho/\Delta z$ (Fig. 1e), representing overall stratification, decreases from summer to fall overall from $6\times$ to $1\times 10^{-4}\,\mathrm{s^{-2}}$, but also has diurnal and semidiurnal fluctuations associated with surface heating/cooling and internal tides (Wu et al. 2020).

c. Analysis methods

Within the nearshore study region, the time- (tides and wave-induced setup) and alongshore varying shoreline location x_{sh} is defined as the location of zero total water depth ($h + \eta = 0$, where η is the sea-surface elevation). Within the nearshore study region, the alongshore averaged (denoted with $\langle\,\rangle$) shoreline location $\langle x_{\mathrm{sh}}\rangle$ has an analysis-period time mean ($\pm$ standard deviation, std) of $0(\pm 7)\,\mathrm{m}$. To account for the time-varying shoreline, a shoreline-referenced cross-shore coordinate is defined as $\tilde{x} = x - \langle x_{\mathrm{sh}}\rangle$. The wave breakpoint cross-shore location x_b (Fig 2a1) is defined as where the depth-limited wave breaking fraction reaches 4% (*e.g.,* Battjes and Stive 1985), which varies largely with incident H_s (Fig. 1b) and the tide. The alongshore-averaged wave breakpoint location $\langle x_b\rangle$ has a time mean of $-96(\pm 45)\,\mathrm{m}$. The surfzone width L_{sz} is defined as the alongshore averaged difference between the shoreline and breakpoint location $L_{\mathrm{sz}} = \langle x_{\mathrm{sh}}\rangle - \langle x_b\rangle$ and has an analysis-period time mean (indicated with an overbar) of $\bar{L}_{\mathrm{sz}} = 96(\pm 41)\,\mathrm{m}$.

We analyze quantities related to flow spatial variability such as relative vertical vorticity $\zeta = \partial v/\partial x - \partial u/\partial y$, divergence $\delta = \partial u/\partial x + \partial v/\partial y$ and cross-shore eddy velocity u', where the prime represents the perturbation from the alongshore averaged flow,

$$u(x,y,z,t) = \langle u\rangle(x,z,t) + u'(x,y,z,t). \tag{1}$$

Vorticity and divergence are normalized by the Coriolis parameter f. The surfzone effects on the inner-shelf are primarily diagnosed by examining the magnitude of flow spatial variability using the alongshore root-mean-square of a variable as (for vorticity),

$$\mathrm{rms}(\zeta/f) = \langle\zeta^2\rangle^{1/2}/f \tag{2}$$

focusing on $\mathrm{rms}(\zeta/f)$, $\mathrm{rms}(\delta/f)$, and $\mathrm{rms}(u')$ which are functions of x, z, and time.

3. Results

a. Example WW and NW model snapshots

Clear differences between the WW (that has a surfzone) and NW (no surfzone) runs can be seen from instantaneous flow and density snapshots, such as those shown on 2100 UTC 12 October (Fig. 2) with weak winds at $3.5\,\mathrm{m\,s^{-1}}$ (Fig. 1b), a relatively low tide ($\eta = -0.4$ m), and relatively large waves. At site S, the WW run $H_s = 1.30\,\mathrm{m}$ at this time, 7 hours after the analysis period maximum $H_s = 1.45\,\mathrm{m}$ (Fig. 1c), with near-normal incident wave angle (not shown). In the nearshore study region, the wave breakpoint x_b is just onshore of the $h = 5\,\mathrm{m}$ isobath (dashed magenta line in Fig. 2a1), and x_b and x_{sh} vary coherently alongshore with a resulting large, alongshore-averaged surfzone width of $L_{\mathrm{sz}} = 236$ m (std of 32 m). In this WW example, the surfzone is generally $\sim 0.2\,\mathrm{kg\,m^{-3}}$ denser than the shelf offshore. Rip currents eject the denser surfzone water onto the inner-shelf, resulting in significant flow and density spatial variability within 1–2 km from shore. We focus on the rip current within the nearshore study region (at 32.5N). This rip current has an offshore directed jet, extending $1.4\,\mathrm{km}$ from the shoreline and crossing the $15\,\mathrm{m}$ isobath, which gradually widens from $0.5\,\mathrm{km}$ at $h = 10$ m to $0.9\,\mathrm{km}$ at $h = 15$ m. This rip current impacts inner-shelf flow variability up to $6L_{\mathrm{sz}}$ from the shoreline. Associated with the density front, the jet leading edge has surface divergence $\delta/f \sim -10$ and, 1 km from shore (or $4L_{\mathrm{sz}}$), surface relative vorticity $\zeta/f \sim \pm 5$ on the cyclonic (south) and anticyclonic (north) sides of the jet (not shown). Inner-shelf impacts over the vertical (z) are also evident on a cross-shore transect aligned with the rip current jet (green-dashed, Fig. 2a1). Onshore of the front at $x = -1.4$ km, u is offshore directed within the upper 5 m (Fig. 2a2), the upper 5-m averaged velocity decreases from $0.2\ \mathrm{m\,s^{-1}}$ at $x = -0.5$ km to $0.05\ \mathrm{m\,s^{-1}}$ at the front, and stratification is weak throughout the water column, reflecting strong rip-current mixing (*e.g.,* Kumar and Feddersen 2017b; Uchiyama et al. 2017). Just offshore of the front, near-surface flow is weakly onshore and the upper 5 m is strongly stratified with vertical density difference of $0.2\,\mathrm{kg\,m^{-3}}$. At this same time, the NW run shelf circulation and density field is strikingly different (Fig. 2b1,b2). The NW surface density and flow variability is weaker and smoother than WW. The surface shelf flows for $h > 5$ m are roughly alongshore uniform which, in $h < 5$ m, weaken due to the shoreline barrier and bottom friction (Fig. 2b1). On the cross-shore transect (green dashed, Fig. 2b1), NW currents have a mode-1 baroclinic structure with weak ($\sim 0.03\,\mathrm{m\,s^{-1}}$) onshore flow over the upper $3\,\mathrm{m}$ and much weaker ($\sim 0.005\,\mathrm{m\,s^{-1}}$) offshore flow underneath (Fig. 2b2). The water column is well stratified over the transect to within 200 m of the shoreline.

Within the nearshore study region, the WW and NW example differences in inner-shelf flow spatial variability are contextualized with alongshore root-mean-square (rms, Section 2c) of surface vorticity, divergence, and cross-shore eddy velocity for this case example (Fig. 2). For example, between 1 km and 1.4 km from the shoreline (about $4L_{\mathrm{sz}}$ to $6L_{\mathrm{sz}}$), the WW $\mathrm{rms}(\zeta/f) \approx 3$, $\mathrm{rms}(\delta/f) \approx 4$ and $\mathrm{rms}(u') \approx 0.065\,\mathrm{m\,s^{-1}}$, indicating strong eddy variability and divergent motions - associated with the submesoscale. In contrast, over the same region (1–1.4 km from shore), the NW $\mathrm{rms}(\zeta/f) \approx 0.66$ and $\mathrm{rms}(\delta/f) \approx 0.3$, far weaker ($6\times$ and $12\times$, respectively) than WW, and their values < 1 indicate different dominant flow dynamics. The NW $\mathrm{rms}(u') \approx 0.005\ \mathrm{m\,s^{-1}}$ is over $10\times$ smaller than for WW. Overall, for this case example, clear surfzone effects on the inner-shelf are present to $6L_{\mathrm{sz}}$ within the nearshore study region.

FIG. 3

FIG. 4

b. WW and NW run inner-shelf flow spatial variability statistics

The WW run example has dramatically more flow spatial variability (impacting vorticity, divergence, and eddy cross-shore velocity) than the NW run, inducing significant density variation (Fig. 2). Here, the WW and NW run differences in flow spatial variability metrics ζ, δ, and u' are examined statistically over the analysis period, quantifying the surfzone effects on the inner-shelf. At each time step surface $\mathrm{rms}(\zeta/f)$, $\mathrm{rms}(\delta/f)$, and $\mathrm{rms}(u')$ are interpolated onto a surfzone-width normalized offshore coordinate $\tilde{x}/L_{\mathrm{sz}}$, as L_{sz} is a key length-scale for inner-shelf rip current effects in idealized models (Suanda and Feddersen 2015), and subsequently the temporal median (50%), 30%, and 70% values are calculated (Fig. 3). In addition, at a selected cross-shore location $\tilde{x}/L_{\mathrm{sz}} = -4$, the temporal median (50%), 30%, and 70% values of flow metrics are calculated over the non-dimensional vertical $z'/(h+\eta)$, where the vertical coordinate is referenced to the sea-surface η, *i.e.,* $z' = z - \eta$ (Fig. 4).

We first examine the normalized cross-shore structure of rms flow spatial variability metrics at the surface (Fig. 3). At the surfzone boundary ($\tilde{x}/L_{\mathrm{sz}} = -1$), the WW median $\mathrm{rms}(\zeta/f)^{(\mathrm{ww})} = 18$, substantially greater than the NW mean $\mathrm{rms}(\zeta/f)^{(\mathrm{nw})} = 3.5$ (Fig. 3a), as expected near the surfzone boundary. The median $\mathrm{rms}(\zeta/f)^{(\mathrm{ww})}$ decays offshore rapidly to about $\tilde{x}/L_{\mathrm{sz}} = -3$ and more slowly farther offshore. In contrast, $\mathrm{rms}(\zeta/f)^{(\mathrm{nw})}$ decays slowly offshore throughout so that by $\tilde{x}/L_{\mathrm{sz}} = -8$ the WW and NW $\mathrm{rms}(\zeta/f) \approx 0.75$ with similar, largely overlapping distributions (Fig. 3a). For WW, the cross-shore structure of $\mathrm{rms}(\delta/f)$ is analogous to vorticity, with a $\tilde{x}/L_{\mathrm{sz}} = -1$ maximum of $\mathrm{rms}(\delta/f)^{(\mathrm{ww})} = 3.5$ and offshore decay that largely merges with the nearly cross-shore uniform $\mathrm{rms}(\delta/f)^{(\mathrm{nw})} \approx 1$ by $\tilde{x}/L_{\mathrm{sz}} = -8$ (Fig. 3b). In the intermediate zone of $-5 < \tilde{x}/L_{\mathrm{sz}} < -3$, $\mathrm{rms}(\zeta/f)^{(\mathrm{ww})}$ and $\mathrm{rms}(\delta/f)^{(\mathrm{ww})}$ are usually elevated over $\mathrm{rms}(\zeta/f)^{(\mathrm{nw})}$ and $\mathrm{rms}(\delta/f)^{(\mathrm{nw})}$, respectively. For example, at $\tilde{x}/L_{\mathrm{sz}} = -4$, the median $\mathrm{rms}(\zeta/f)^{(\mathrm{ww})} = 2.8$ whereas $\mathrm{rms}(\zeta/f)^{(\mathrm{nw})} = 1.4$ and $\mathrm{rms}(\zeta/f)^{(\mathrm{ww})} > \mathrm{rms}(\zeta/f)^{(\mathrm{nw})}$ 82% of the time (Fig. 3a). Similarly, at $\tilde{x}/L_{\mathrm{sz}} = -4$, the median $\mathrm{rms}(\delta/f)^{(\mathrm{ww})} = 1.8$ whereas the median $\mathrm{rms}(\zeta/f)^{(\mathrm{nw})} = 1.0$, and $\mathrm{rms}(\delta/f)^{(\mathrm{ww})} > \mathrm{rms}(\delta/f)^{(\mathrm{nw})}$ 81% of the time (Fig. 3b). The cross-shore structure of WW and NW $\mathrm{rms(u')}$ are qualitatively similar to the vorticity and divergence metrics (Fig. 3c). The $\mathrm{rms(u')}^{(\mathrm{ww})}$ decays strongly offshore from a $\tilde{x}/L_{\mathrm{sz}} = -1$ maximum of $\mathrm{rms(u')}^{(\mathrm{ww})} = 0.035\ \mathrm{m\,s^{-1}}$ down to $\mathrm{rms(u')}^{(\mathrm{ww})} = 0.013\ \mathrm{m\,s^{-1}}$ at $\tilde{x}/L_{\mathrm{sz}} = -10$. In contrast, $\mathrm{rms(u')}^{(\mathrm{nw})}$ is largely $0.01\ \mathrm{m\,s^{-1}}$ and decays slightly towards the shoreline (Fig. 3c) due to no surfzone forcing and shallow water friction. Over $-6 < \tilde{x}/L_{\mathrm{sz}} < -3$, the $\mathrm{rms(u')}^{(\mathrm{ww})}$ is consistently larger than $\mathrm{rms(u')}^{(\mathrm{nw})}$. For example, at $\tilde{x}/L_{\mathrm{sz}} = -4$, mean $\mathrm{rms(u')}^{(\mathrm{ww})} = 0.018\ \mathrm{m\,s^{-1}}$ whereas the median $\mathrm{rms(u')}^{(\mathrm{nw})} = 0.009\ \mathrm{m\,s^{-1}}$, and $\mathrm{rms(u')}^{(\mathrm{ww})} > \mathrm{rms(u')}^{(\mathrm{nw})}$ 90% of the time.

These results show that, over the three-month analysis period, the temporal median of the three rms flow spatial variability metrics at the surface are consistently elevated out to $\tilde{x}/L_{\mathrm{sz}} \approx -5$. We define the region where the surfzone consistently affects the inner-shelf as where the WW metric exceeds the NW metric $\geq 70\%$ of the time. This location is similar for all three metrics at the surface and is bounded by $\tilde{x}/L_{\mathrm{sz}} = -5.5$ for $\mathrm{rms}(\zeta/f)$ and $\mathrm{rms}(\delta/f)$ and is bounded by

$\tilde{x}/L_{\rm sz} = -6.3$ for $\mathrm{rms}(\mathrm{u}')$, confirming that the region onshore of $\tilde{x}/L_{\rm sz} = -5$ as that of consistent surfzone impacts on inner-shelf flow spatial variability. Of course, surfzone effects can and do extend farther offshore such as in the case example in Fig. 2a, but do not do so consistently.

Next, we examine the vertical structure of the WW and NW flow spatial variability metrics at $\tilde{x}/L_{\rm sz} = -4$, a location relatively far offshore where the surface WW metrics are consistently larger than NW. For reference, at $\tilde{x}/L_{\rm sz} = -4$, the water depth $(h + \eta)$ varies from $6.9(\pm 2.3)$ m. The WW median $\mathrm{rms}(\zeta/f)$ decreases from near-surface $\mathrm{rms}(\zeta/f)^{(\rm ww)} = 2.7$ to near-bed $\mathrm{rms}(\zeta/f)^{(\rm ww)} = 2.0$ (Fig. 4a). In contrast the NW $\mathrm{rms}(\zeta/f)$ has subsurface maxima ≈ 1.8 at $z'/(h + \eta) = -0.6$, resulting in WW to NW $\mathrm{rms}(\zeta/f)$ median ratio of 1.4. The WW to NW $\mathrm{rms}(\zeta/f)$ ratio is > 1 more than 70% of the time everywhere in the water column. The WW median $\mathrm{rms}(\delta/f)^{(\rm ww)}$ varies from near-surface ≈ 1.7 to near-bed ≈ 1.3 (Fig. 4b). The NW median $\mathrm{rms}(\delta/f)$ varies similarly in the vertical and is within 0.5–0.7 of $\mathrm{rms}(\delta/f)^{(\rm ww)}$. The WW and NW distributions overlap somewhat, but everywhere in the water column the WW to NW $\mathrm{rms}(\delta/f)$ ratio is > 1 more than 70% of the time. The $\mathrm{rms}(\mathrm{u}')^{(\rm ww)}$ decays with depth from $0.017\ \mathrm{m\,s^{-1}}$ to $0.010\ \mathrm{m\,s^{-1}}$ whereas $\mathrm{rms}(\mathrm{u}')^{(\rm nw)}$ is more vertically uniform varying from 0.07–$0.08\ \mathrm{m\,s^{-1}}$ (Fig. 4c). The median WW to NW $\mathrm{rms}(\mathrm{u}')$ ratio decreases from 2 near-surface to 1.3 near-bed. Throughout most of the water column the $\mathrm{rms}(\mathrm{u}')^{(\rm ww)}/\mathrm{rms}(\mathrm{u}')^{(\rm nw)} > 1$ more than 80% of the time. Thus, the larger WW relative to NW surface flow spatial variability metrics at $\tilde{x}/L_{\rm sz} = -4$ are also largely consistent throughout the water column (Fig. 4), although WW and NW median flow metrics are more similar with increased distribution overlap near the bed. The differences over the water column in WW and NW flow spatial variability metrics increase rapidly onshore (not shown), as at the surface (Fig. 3).

c. WW and NW eddy cross-shore velocity correlations in a fixed cross-shore coordinate

FIG. 5

Surfzone effects on the inner-shelf out to $5L_{\rm sz}$ are consistently seen in the magnitude (root-mean-square) of the metrics ζ/f, δ/f, and u' representing flow spatial variability. These metrics are linked to the cross-shore eddy tracer transport at a fixed location (*i.e.,* $\overline{u'C'}$, where C is a generic tracer), which depends both on u' magnitude and its correlation with tracer fluctuations. Even if the NW and WW runs have similar $\mathrm{rms}(u')$, a non unitary correlation between WW and NW u' suggests differences in eddy cross-shore transport and in Lagrangian tracer evolution. As eddy transport is calculated at a fixed location (*e.g.,* with an ADCP and mooring), we examine the surface u' squared correlation r^2 between WW and NW runs in a fixed coordinate system, not a $L_{\rm sz}$ normalized (moving) coordinate system. Within 0.2 km of shore (or $\approx 2\bar{L}_{\rm sz}$, where the time-average $\bar{L}_{\rm sz} = 96$ m), the u' squared correlation r^2 between WW and NW runs is near-zero (Fig. 5), as expected near the surfzone, where strong surfzone currents are driven in the WW run. Farther offshore, the u' r^2 between WW and NW runs increases quasi-linearly to about $r^2 = 0.46$ at $x = -1.2$ km (or $\approx 12\bar{L}_{\rm sz}$, Fig. 5), indicating significant differences in timing or phase of u' between WW and NW runs. The cross-shore structure of the squared correlations between WW and NW for ζ/f and δ/f are similar (not shown). Thus, although the NW and WW eddy cross-shore velocities have largely similar magnitudes far offshore (Fig. 3c), their significant non-zero correlation at $12\bar{L}_{\mathrm{sz}}$ (Fig. 5) indicates that, cross-shore eddy transport is likely different even 1 km offshore for a model that includes surfzone effects relative to one that does not.

4. Discussion

a. *Effect of inner-shelf processes on WW and NW metrics*

FIG. 6

We have statistically demonstrated surfzone effects on the inner-shelf out to $5L_{\mathrm{sz}}$ using differences between the modeled WW and NW magnitude metrics of flow spatial variability (vorticity, divergence, and eddy cross-shore velocity, Figs. 3,4) as well as the eddy cross-shore velocity squared correlation between the WW and NW runs (Fig. 5). At $\tilde{x}/L_{\mathrm{sz}} = -4$ the WW surface flow spatial variability metrics are $> 80\%$ likely to be larger than for NW. However occasional times exist where, for example $\mathrm{rms}(\zeta/f)^{(\mathrm{nw})} > \mathrm{rms}(\zeta/f)^{(\mathrm{ww})}$ at $\tilde{x}/L_{\mathrm{sz}} = -4$. Various inner-shelf mechanisms, for example inner-shelf eddies or mean flow may impact the cross-shore distance that surfzone ejected vorticity can impact the inner-shelf. Here, we examine the effect of hourly depth-averaged alongshelf velocity at location S, V_{S} (Fig. 1d), on the ratio $\mathrm{rms}(\zeta/f)^{(\mathrm{ww})}/\mathrm{rms}(\zeta/f)^{(\mathrm{nw})}$ at the normalized cross-shore location $\tilde{x}/L_{\mathrm{sz}} = -4$ (Fig. 6). For weak $|V_{\mathrm{S}}| < 0.1\ \mathrm{m\,s^{-1}}$, the median $\mathrm{rms}(\zeta/f)^{(\mathrm{ww})}/\mathrm{rms}(\zeta/f)^{(\mathrm{nw})}$ is always ≥ 1.7 and the $\mathrm{rms}(\zeta/f)^{(\mathrm{ww})}/\mathrm{rms}(\zeta/f)^{(\mathrm{nw})}$ is very often (87%) greater than one. However, the median $\mathrm{rms}(\zeta/f)^{(\mathrm{ww})}/\mathrm{rms}(\zeta/f)^{(\mathrm{nw})}$ decreases with increasing V_{S} from a maximum of 2.7 at $V_{\mathrm{S}} = 0.035\ \mathrm{m\,s^{-1}}$ to ≈ 1.25 for $V_{\mathrm{S}} = 0.25\ \mathrm{m\,s^{-1}}$ with narrowing ratio distributions. For $V_{\mathrm{S}} \geq 0.2\ \mathrm{m\,s^{-1}}$, $\mathrm{rms}(\zeta/f)^{(\mathrm{ww})}/\mathrm{rms}(\zeta/f)^{(\mathrm{nw})} > 1$ only 62% of the time, or close to equal probability. Thus, the cross-shore extent of surfzone effects on the inner-shelf are reduced for stronger alongshelf flows. Note, large V_{S} are relatively uncommon (Fig. 1d). This result is consistent with alongshelf flows reducing the offshore extent of observed and modeled drifters released within a BRC (Winter et al. 2014). Other shelf processes may impact the relative strength of the WW to NW flow spatial variability metrics. For example, a warmer surfzone relative to inner-shelf leads to farther offshore rip current propagation in both observations and models (Moulton et al. 2020). In addition, nonlinear internal waves (NLIW) are active in this region's inner-shelf (*e.g.,* Grimes et al. 2019), can propagate to the surfzone (Sinnett et al. 2018), and have an associated surface horizontal divergence. The relative importance of rip current induced surface divergence (*e.g.,* Fig. 2a1) would be reduced during times of NLIW events resulting in smaller ratio of $\mathrm{rms}(\delta/f)^{(\mathrm{ww})}/\mathrm{rms}(\delta/f)^{(\mathrm{nw})}$.

b. *Surfzone vorticity generation mechanisms*

The COAWST model with coupled ROMS and SWAN does not have wave group (*e.g.,* Long and Özkan-Haller 2009) or finite-crest length breaking (Clark et al. 2012) surfzone vorticity generation mechanisms that generate transient rip currents (TRCs) particularly at relatively short (10–50 m) alongshore length-scales (Feddersen 2014). Instead surfzone vorticity is generated through alongshore bathymetric variations (BRCs) and shear instabilities (*e.g.,* Noyes et al. 2005). The model horizontal eddy viscosity of $0.5\,\mathrm{m}^2\,\mathrm{s}^{-1}$ is sufficiently small to allow shear instabilities to occur (Özkan-Haller and Kirby 1999). A model study that resolves both BRCs and TRCs reveals that both of them are important contributors to the total eddy kinetic energy (*i.e.,* $\langle u'^2\rangle + \langle v'^2\rangle$) (O'Dea et al. 2020). As the wave group and finite-crest length breaking vorticity generation mechanisms that induce TRCs are not included, the model results here likely represent a lower bound on surfzone effects on the inner-shelf. For example, for similar incident waves, an idealized, TRC-resolving COAWST simulation had $\mathrm{rms}(\zeta/f) \approx 40$ at $\tilde{x}/L_{\mathrm{sz}} = -2$ (Kumar and Feddersen 2017a), significantly larger than the median $\mathrm{rms}(\zeta/f)^{(\mathrm{ww})} = 11$ (Fig. 3a) or the 90% value of 18.

The nearshore study region (red box in Fig. 2) was chosen for its relatively alongshore uniform bathymetry. However, offshore of the surfzone, bathymetric variations are sufficient to induce, via wave refraction, alongshore variations in the breakpoint (dashed magenta in Fig. 2a1) that induce convergent surfzone alongshore currents and BRCs (Long and Özkan Haller 2005). In addition, bathymetry within the surfzone is alongshore variable as quantified by the metric $\langle h'^2\rangle/\langle h\rangle^2 \approx 0.12$, a value indicating alongshore nonuniform circulation (Ruessink et al. 2001; Feddersen and Guza 2003) which can induce BRCs (Apotsos et al. 2008), even for a uniform incident wave field.

Lastly, within the nearshore study region, the cross-shore model resolution is relatively coarse, on average within the nearshore study region $\Delta x = 18$ m, and as such the model resolution in the surfzone is limited. This model resolution was a compromise between spanning more than 10 km offshore (Fig. 1a) and resolving the surfzone (Fig. 2a1). On the inner-shelf, increased model resolution has been shown to significantly enhance submesoscale processes and cross-shelf transport (Dauhajre et al. 2019). Increased model resolution within the nearshore study region also is likely to enhance the surfzone effects on the inner-shelf as diagnosed by the flow spatial variability metrics.

c. Other surfzone effects on the inner-shelf

As rip currents are ejected from the surfzone onto the inner-shelf inducing vorticity and eddies on the inner-shelf, we have examined the magnitude of three flow spatial variability metrics, related to eddies and eddy transport, and their difference between the WW and NW runs. As the $\mathrm{rms}(u')$ varies strongly (*i.e.,* is inhomogeneous) cross-shore, the cross-shore extent of eddy transport is limited as long-time dispersion is subdiffusive in a spatially-inhomogeneous eddy field (Spydell et al. 2019). Rip currents can have other impacts on the inner-shelf. The enhanced vertical mixing within TRCs on the stratified inner-shelf induces a cross-shore circulation cell transporting subsurface low stratified water and tracer $\sim 10L_{\mathrm{sz}}$ offshore in ~ 12 h for incident $H_{\mathrm{s}} = 1$ m (Kumar and Feddersen 2017c). This mechanism is self-similar, depends on stratification and rip current eddy kinetic energy flux, and offshore of $\sim 4L_{\mathrm{sz}}$ is far more effective at cross-shelf transport than eddy transport (Grimes and Feddersen 2020). However, note that the COAWST model does not include TRC effects. BRCs also enhance vertical mixing (Uchiyama et al. 2017), but their effect on inner-shelf stratification is not yet studied. The surfzone may have many other effects on the inner-shelf. For example a rip current jet may refract an incident inner-shelf NLIW resulting in alongshore variable NLIW dissipation and tracer transport. Rip current induced density gradients may seed submesoscale density fronts, particularly in a pre-existing shelf strain field (Wu et al. 2020). On a realistic inner-shelf with overlapping processes, diagnosing such effects requires separating out internal waves, diurnal forced oscillations (Grimes et al. 2020), and rip current forced processes, which will be the subject of future work.

d. Effects on the inner-shelf in other regions

We have shown consistent surfzone effects on the inner-shelf out to $5L_{\mathrm{sz}}$ from the shoreline for the magnitude of flow spatial variability metrics (Fig. 3). Thus, ocean models that do not include surfzone processes will under-represent eddy processes within this region. During this 3-month long simulation, the significant wave height H_{s} was fairly small, ≤ 1 m the majority (85%) of the time and the maximum wave height $H_{\mathrm{s}} = 1.45$ m (Fig. 1b). The resulting $\bar{L}_{\mathrm{sz}} = 96$ m (and mostly < 150 m). With surfzone effects to $5L_{\mathrm{sz}}$, this implies effects on average out to 500 m (mostly < 750 m) from shore. In many other regions, the incident H_{s} is much larger. For example, during winter time on the Oregon US coast, incident H_{s} is very often ≥ 3 m and can be as large as 9 m (Seymour et al. 2016). Assuming a planar bathymetry so that L_{sz} increases linearly with H_{s}, this suggests that surfzone effects on the inner-shelf can extend multiple km offshore during such large waves, whose inner-shelf impacts are not understood. Typical realistic coastal ocean circulation models that neglect surfzone effects use a horizontal grid resolution of 200 m (Romero et al. 2013; Suanda et al. 2017; Kumar et al. 2019) to 75 m (Dauhajre et al. 2017), and so multiple near-shoreline model grid points will be impacted, affecting transport and dispersion of larvae, pollutants, or other tracers across the inner-shelf and surfzone region.

Summary

Surfzone generated rip currents eject vorticity onto the inner-shelf inducing flow spatial variability. This work investigates the surfzone effects on inner-shelf flow spatial variability using two nearly identical twin realistic simulations of the San Diego Bight over the summer to fall transition. One simulation (WW) uses a wave-current coupled model whereas another (NW) does not include waves. The three-month analysis period is characterized by weak to moderate winds, weak to moderate (usually < 1 m) incident significant wave height, diurnal heating and cooling, active internal waves, and submesoscale frontal processes. An example of the modeled density and flow snapshots show dramatic differences between the WW and NW runs, as the WW run has rip currents that extend up to six surf zone widths L_{sz} from the shoreline inducing flow spatial variability. Flow spatial variability metrics, defined as alongshore root-mean-square vorticity, divergence, and eddy cross-shore velocity, are analyzed in a $L_{\rm sz}$ normalized cross-shore coordinate, where $L_{\rm sz}$ is time varying and has a time average of $96(\pm 41)$ m. At the surface, the three metrics are consistently ($> 70\%$ of the time) elevated in the WW run relative to NW out to $5L_{\rm sz}$ offshore. At $4L_{\rm sz}$ offshore, a location relatively far offshore, metrics are enhanced in the WW run over the entire water column although WW and NW metrics are more similar near the bed. In a fixed coordinate as used for eddy transport analysis, the eddy cross-shore velocity squared correlation between WW and NW runs is near-zero within 0.2 km of shore, and is < 0.5 out to 1.2 km offshore or 12 time-averaged $L_{\rm sz}$. These results indicate that the transport and dispersion of tracers (*e.g.,* heat, larvae and pollutants) across the inner-shelf will be significantly different in the WW relative to NW runs.

The relative strength of the WW and NW metrics within the inner shelf is also affected by the shelf alongshore flows, as the WW and NW vorticity is more likely to be similar for stronger shelf alongshore flows. The phase-averaged wave model used here has bathymetrically controlled and shear instability induced rip currents, but does not have wave group or finite crest length breaking induced rip currents. Thus, surfzone effects on the inner shelf flow variability is likely underestimated here. Other coastal regions experience much larger incident waves than in this simulation, which will result in surfzone impacts that extend much farther offshore, distances multiple grid points of realistic ocean models that do not include waves. To model the realistic transport and dispersion of tracers (*e.g.,* larvae, pollutants) across the inner-shelf, wave-forced surfzone processes need to be included.

Acknowledgments. This work was supported by the National Science Foundation (OCE-1459389) as part of the Cross-Surfzone/Inner-shelf Dye Exchange (CSIDE) experiment. Additional funding is through the Environmental Protection Agency through the North American Development Bank, however it does not necessarily reflect the policies, actions or positions of the U.S. EPA or NADB. This work used the Extreme Science and Engineering Discovery Environment (XSEDE), which is supported by National Science Foundation (ACI-1548562). The numerical simulations were performed on the comet cluster at the San Diego Super Computer Center through XSEDE allocation TG-OCE180013. NOAA provided the NAM atmospheric forcing fields and the bathymetry. SIO Coastal Data Information Program provided wave forcing. Ganesh Gopalakrishnan and Bruce Cornuelle provided CASE model solutions for outer grid boundary conditions which are available online (http://ecco.ucsd.edu/case.html). We also appreciate extra support from the Tijuana River National Estuarine Research Reserve and the Southern California Coastal Ocean Observing System. Derek Grimes, Angelica Rodriguez and Elizabeth Brasseale provided useful feedback on this work. This work is inspired by and dedicated to the memory of our dear friend and colleague Nirnimesh Kumar.

REFERENCES

Apotsos, A., B. Raubenheimer, S. Elgar, and R. T. Guza, 2008: Wave-driven setup and alongshore flows observed onshore of a submarine canyon. *Journal of Geophysical Research: Oceans*, **113**, doi:10.1029/2007JC004514.

Austin, J. A., and S. J. Lentz, 2002: The inner shelf response to wind-driven upwelling and downwelling. *Journal of Physical Oceanography*, **32**, 2171–2193.

Battjes, J., 1988: Surf-zone dynamics. *Annual Review of Fluid Mechanics*, **20**, 257–291.

Battjes, J. A., and M. J. F. Stive, 1985: Calibration and verification of a dissipation model for random breaking waves. *Journal of Geophysical Research: Oceans*, **90**, doi:https://doi.org/10.1029/JC090iC05p09159, 9159–9167.

Booij, N., R. C. Ris, and L. H. Holthuijsen, 1999: A third-generation wave model for coastal regions: 1. model description and validation. *Journal of Geophysical Research: Oceans*, **104**, doi:10.1029/98JC02622, 7649–7666.

Brink, K., 2016: Cross-shelf exchange. *Annual Review of Marine Science*, **8**, doi:10.1146/annurev-marine-010814-015717, 59–78.

Brown, J. A., J. H. MacMahan, A. J. H. M. Reniers, and E. B. Thornton, 2015: Field Observations of Surf Zone–Inner Shelf Exchange on a Rip-Channeled Beach. *Journal of Physical Oceanography*, **45**, doi:10.1175/JPO-D-14-0118.1, 2339–2355.

Castelao, R., R. Chant, S. Glenn, and O. Schofield, 2010: The Effects of Tides and Oscillatory Winds on the Subtidal Inner-Shelf Cross-Shelf Circulation. *Journal of Physical Oceanography*, **40**, doi:10.1175/2009JPO4273.1, 775–788.

Castelle, B., and G. Coco, 2013: Surf zone flushing on embayed beaches. *Geophysical Research Letters*, **40**, doi:10.1002/grl.50485, 2206–2210.

Castelle, B., A. Reniers, and J. MacMahan, 2014: Bathymetric control of surf zone retention on a rip-channelled beach. *Ocean Dynamics*, **64**, doi:10.1007/s10236-014-0747-0, 1221–1231.

Clark, D. B., S. Elgar, and B. Raubenheimer, 2012: Vorticity generation by short-crested wave breaking. *Geophys. Res. Lett.*, **39**, doi:10.1028/2012GL054034.

Dalrymple, R., J. MacMahan, A. J. Reniers, and V. Nelko, 2011: Rip currents. *Annual Review of Fluid Mechanics*, **43**, doi:10.1146/annurev-fluid-122109-160733, 551–581.

Dauhajre, D. P., J. C. McWilliams, and L. Renault, 2019: Nearshore lagrangian connectivity: Submesoscale influence and resolution sensitivity. *Journal of Geophysical Research: Oceans*, **124**, 5180–5204.

Dauhajre, D. P., J. C. McWilliams, and Y. Uchiyama, 2017: Submesoscale coherent structures on the continental shelf. *Journal of Physical Oceanography*, **47**, doi:10.1175/JPO-D-16-0270.1, 2949–2976.

Davis, K. A., R. S. Arthur, E. C. Reid, J. S. Rogers, O. B. Fringer, T. M. DeCarlo, and A. L. Cohen, 2020: Fate of internal waves on a shallow shelf. *Journal of Geophysical Research: Oceans*, **125**, doi:https://doi.org/10.1029/2019JC015377, e2019JC015377.

Feddersen, F., 2012: Scaling surf zone turbulence. *Geophysical Research Letters*, **39**, doi:10.1029/2012GL052970.

— 2014: The generation of surfzone eddies in a strong alongshore current. *Journal of Physical Oceanography*, **44**, doi:10.1175/JPO-D-13-051.1, 600–617.

Feddersen, F., and R. T. Guza, 2003: Observations of nearshore circulation: Alongshore uniformity. *Journal of Geophysical Research: Oceans*, **108**, doi:10.1029/2001JC001293.

Feddersen, F., R. T. Guza, S. Elgar, and T. H. C. Herbers, 1998: Alongshore momentum balances in the nearshore. *Journal of Geophysical Research: Oceans*, **103**, doi:10.1029/98JC01270, 15667–15676.

Fewings, M., S. J. Lentz, and J. Fredericks, 2008: Observations of cross-shelf flow driven by cross-shelf winds on the inner continental shelf. *Journal of Physical Oceanography*, **38**, doi:10.1175/2008JPO3990.1, 2358–2378.

Ganju, N. K., S. J. Lentz, A. R. Kirincich, and J. T. Farrar, 2011: Complex mean circulation over the inner shelf south of martha's vineyard revealed by observations and a high-resolution model. *Journal of Geophysical Research: Oceans*, **116**, doi:10.1029/2011JC007035.

Grimes, D. J., and F. Feddersen, 2020: The self-similar stratified inner-shelf response to transient rip-current induced mixing. *J. Fluid Mech.*, submitted.

Grimes, D. J., F. Feddersen, S. N. Giddings, and G. Pawlak, 2019: Cross-shore deformation of a surfzone-released dye plume by an internal tide on the inner shelf. *Journal of Physical Oceanography*, **50**, doi:10.1175/JPO-D-19-0046.1, 35–54.

Grimes, D. J., F. Feddersen, and N. Kumar, 2020: Tracer exchange across the stratified inner-shelf driven by transient rip-currents and diurnal surface heat fluxes. *Geophysical Research Letters*, **47**, doi:10.1029/2019GL086501, e2019GL086501.

Haller, M. C., R. A. Dalrymple, and I. A. Svendsen, 2002: Experimental study of nearshore dynamics on a barred beach with rip channels. *Journal of Geophysical Research: Oceans*, **107**, doi:10.1029/2001JC000955, 14–1–14–21.

Hally-Rosendahl, K., F. Feddersen, D. B. Clark, and R. T. Guza, 2015: Surfzone to inner-shelf exchange estimated from dye tracer balances. *Journal of Geophysical Research: Oceans*, doi:10.1002/2015JC010844, n/a–n/a.

Hally-Rosendahl, K., F. Feddersen, and R. T. Guza, 2014: Cross-shore tracer exchange between the surfzone and inner-shelf. *Journal of Geophysical Research: Oceans*, **119**, doi:10.1002/2013JC009722, 4367–4388.

Horwitz, R., and S. J. Lentz, 2014: Inner-shelf response to cross-shelf wind stress: The importance of the cross-shelf density gradient in an idealized numerical model and field observations. *Journal of Physical Oceanography*, **44**, doi:10.1175/JPO-D-13-075.1, 86 – 103.

Johnson, D., and C. Pattiaratchi, 2006: Boussinesq modelling of transient rip currents. *Coastal Engineering*, **53**, doi:10.1016/j.coastaleng.2005.11.005, 419–439.

Kirincich, A., 2016: The occurrence, drivers, and implications of submesoscale eddies on the martha?s vineyard inner shelf. *Journal of Physical Oceanography*, **46**, doi:10.1175/JPO-D-15-0191.1, 2645 – 2662.

Kirincich, A. R., S. J. Lentz, and J. A. Barth, 2009: Wave-driven inner-shelf motions on the oregon coast*. *Journal of Physical Oceanography*, **39**, doi:10.1175/2009JPO4041.1, 2942–2956.

Kumar, N., and F. Feddersen, 2017a: The effect of stokes drift and transient rip currents on the inner shelf. part i: No stratification. *Journal of Physical Oceanography*, **47**, doi:10.1175/JPO-D-16-0076.1, 227–241.

— 2017b: The effect of stokes drift and transient rip currents on the inner shelf. part ii: With stratification. *Journal of Physical Oceanography*, **47**, doi:10.1175/JPO-D-16-0077.1, 243–260.

— 2017c: A new offshore transport mechanism for shoreline-released tracer induced by transient rip currents and stratification. *Geophysical Research Letters*, **44**, doi:10.1002/2017GL072611, 2843–2851.

Kumar, N., F. Feddersen, S. Suanda, Y. Uchiyama, and J. McWilliams, 2016: Mid- to inner-shelf coupled roms?swan model?data comparison of currents and temperature: Diurnal and semidiurnal variability. *Journal of Physical Oceanography*, **46**, doi:10.1175/JPO-D-15-0103.1, 841 – 862.

Kumar, N., F. Feddersen, Y. Uchiyama, J. McWilliams, and W. O'Reilly, 2015: Midshelf to surfzone coupled roms–swan model data comparison of waves, currents, and temperature: Diagnosis of subtidal forcings and response. *Journal of Physical Oceanography*, **45**, doi:10.1175/JPO-

D-14-0151.1, 1464–1490.

Kumar, N., S. H. Suanda, J. A. Colosi, K. Haas, E. Di Lorenzo, A. J. Miller, and C. A. Edwards, 2019: Coastal semidiurnal internal tidal incoherence in the santa maria basin, california: Observations and model simulations. *Journal of Geophysical Research: Oceans*, **124**, doi:10.1029/2018JC014891, 5158–5179.

Kumar, N., G. Voulgaris, W. J., and O. M., 2012: Implementation of the vortex force formalism in the coupled ocean-atmosphere-wave-sediment transport (coawst) modeling system for inner shelf and surf zone applications. *Ocean Modelling*, **47**, doi:10.1016/j.ocemod.2012.01.003, 65 – 95.

Largier, J. L., 2020: Upwelling bays: How coastal upwelling controls circulation, habitat, and productivity in bays. *Annual Review of Marine Science*, **12**, doi:10.1146/annurev-marine-010419-011020, 415–447.

Lentz, S. J., 2001: The influence of stratification on the wind-driven cross-shelf circulation over the north carolina shelf*. *Journal of Physical Oceanography*, **31**, doi:10.1175/1520-0485(2001)031¡2749:TIOSOT¿2.0.CO;2, 2749–2760.

Lentz, S. J., M. Fewings, P. Howd, J. Fredericks, and K. Hathaway, 2008: Observations and a model of undertow over the inner continental shelf. *Journal of Physical Oceanography*, **38**, doi:10.1175/2008JPO3986.1, 2341–2357.

Lentz, S. J., and M. R. Fewings, 2012: The wind- and wave-driven inner-shelf circulation. *Annual Review of Marine Science*, **4**, doi:10.1146/annurev-marine-120709-142745, 317–343.

Long, J. W., and H. Özkan Haller, 2005: Offshore controls on nearshore rip currents. *Journal of Geophysical Research: Oceans*, **110**, doi:10.1029/2005JC003018.

Long, J. W., and H. T. Özkan-Haller, 2009: Low-frequency characteristics of wave group–forced vortices. *Journal of Geophysical Research: Oceans*, **114**, doi:https://doi.org/10.1029/2008JC004894.

Longuet-Higgins, M. S., 1970: Longshore currents generated by obliquely incident sea waves: 1. *Journal of Geophysical Research (1896-1977)*, **75**, doi:10.1029/JC075i033p06778, 6778–6789.

MacMahan, J., J. Brown, J. Brown, E. Thornton, A. Reniers, T. Stanton, M. Henriquez, E. Gallagher, J. Morrison, M. Austin, T. M., and S. N., 2010: Mean lagrangian flow behavior on an open coast rip-channeled beach: A new perspective. *Marine Geology*, **268**, doi:10.1016/j.margeo.2009.09.011, 1 – 15.

Monismith, S. G., A. Genin, M. A. Reidenbach, G. Yahel, and J. R. Koseff, 2006: Thermally driven exchanges between a coral reef and the adjoining ocean. *Journal of Physical Oceanography*, **36**, doi:10.1175/JPO2916.1, 1332 – 1347.

Moulton, M., C. Chickadel, and J. Thomson, 2020: Warm and cool nearshore plumes connecting the surfzone to the inner shelf. *Geophysical Res. Letters*, submitted.

Moulton, M., S. Elgar, B. Raubenheimer, J. C. Warner, and N. Kumar, 2017: Rip currents and alongshore flows in single channels dredged in the surf zone. *Journal of Geophysical Research: Oceans*, **122**, doi:10.1002/2016JC012222, 3799–3816.

Noyes, T. J., R. T. Guza, F. Feddersen, S. Elgar, and T. H. C. Herbers, 2005: Model-data comparisons of shear waves in the nearshore. **110**, C05019.

O'Dea, A., N. Kumar, and M. C. Haller, 2020: Simulations of the surf zone eddy field and cross-shore exchange on a non-idealized bathymetry. *Journal of Geophysical Research: Oceans*, submitted.

O'Reilly, W., C. Olfe, J. Thomas, R. Seymour, and R. Guza, 2016: The california coastal wave monitoring and prediction system. *Coastal Engineering*, **116**, doi:https://doi.org/10.1016/j.coastaleng.2016.06.005, 118 – 132.

Özkan-Haller, H., and J. T. Kirby, 1999: Nonlinear evolution of shear instabilities of the longshore current: A comparison of observations and computations. *Journal of Geophysical Research: Oceans*, **104**, 25,953–25,984.

Peregrine, D., 1998: Surf zone currents. *Theoretical and Computational Fluid Dynamics*, **10**, doi:10.1007/s001620050065, 295–309.

Reniers, A. J. H. M., J. H. MacMahan, E. B. Thornton, and T. P. Stanton, 2007: Modeling of very low frequency motions during RIPEX. *Journal of Geophysical Research: Oceans*, **112**, doi:10.1029/2005JC003122, 3161–3172.

Reniers, A. J. H. M., J. H. MacMahan, E. B. Thornton, T. P. Stanton, M. Henriquez, J. W. Brown, J. A. Brown, and E. Gallagher, 2009: Surf zone surface retention on a rip-channeled beach. *J. Geophys. Res.*, **114**, doi:10.1029/2008JC005153.

Reniers, A. J. H. M., J. A. Roelvink, and E. B. Thornton, 2004: Morphodynamic modeling of an embayed beach under wave group forcing. *Journal of Geophysical Research: Oceans*, **109**, doi:https://doi.org/10.1029/2002JC001586.

Romero, L., Y. Uchiyama, J. C. Ohlmann, J. C. McWilliams, and D. A. Siegel, 2013: Simulations of nearshore particle-pair dispersion in southern california. *Journal of Physical Oceanography*, **43**, doi:10.1175/JPO-D-13-011.1, 1862–1879.

Ruessink, B. G., J. R. Miles, F. Feddersen, R. T. Guza, and S. Elgar, 2001: Modeling the alongshore current on barred beaches. *Journal of Geophysical Research: Oceans*, **106**, 22,451–22,463.

Seymour, R. J., J. O. Thomas, and D. Castel, 2016: Cdip wave observations during a strong el niño year. *Journal of Geophysical Research: Oceans*, **84**, 36–37.

Shchepetkin, A., and J. McWilliams, 2005: The regional oceanic modeling system (roms): a split-explicit, free-surface, topography-following-coordinate oceanic model. *Ocean Modelling*, **9**, doi:10.1016/j.ocemod.2004.08.002, 347 – 404.

Sinnett, G., F. Feddersen, A. J. Lucas, G. Pawlak, and E. Terrill, 2018: Observations of nonlinear internal wave run-up to the surfzone. *Journal of Physical Oceanography*, **48**, doi:10.1175/JPO-D-17-0210.1, 531 – 554.

Spydell, M., and F. Feddersen, 2009: Lagrangian drifter dispersion in the surf zone: Directionally spread, normally incident waves. *Journal of Physical Oceanography*, **39**, doi:10.1175/2008JPO3892.1, 809–830.

Spydell, M. S., F. Feddersen, and S. Suanda, 2019: Inhomogeneous turbulent dispersion across the nearshore induced by surfzone eddies. *Journal of Physical Oceanography*, **49**, doi:10.1175/JPO-D-18-0102.1, 1015–1034.

Suanda, S. H., and F. Feddersen, 2015: A self-similar for cross-shelf exchange driven by transient rip currents. *Geophysical Research Letters*, **42**, doi:10.1002/2015GL063944, 5427–5434.

Suanda, S. H., F. Feddersen, and N. Kumar, 2017: The effect of barotropic and baroclinic tides on coastal stratification and mixing. *Journal of Geophysical Research: Oceans*, **122**, doi:10.1002/2017JC013379, 10156–10173.

Suanda, S. H., F. Feddersen, M. S. Spydell, and N. Kumar, 2018: The effect of barotropic and baroclinic tides on three-dimensional coastal dispersion. *Geophysical Research Letters*, **45**, doi:10.1029/2018GL079884, 11,235–11,246.

Uchiyama, Y., J. C. McWilliams, and C. Akan, 2017: Three-dimensional transient rip currents: Bathymetric excitation of low-frequency intrinsic variability. *Journal of Geophysical Research: Oceans*, **122**, doi:10.1002/2017JC013005, 5826–5849.

Warner, J. C., B. Armstrong, R. He, and J. B. Zambon, 2010: Development of a coupled ocean–atmosphere–wave–sediment transport (coawst) modeling system. *Ocean Modelling*, **35**, doi:10.1016/j.ocemod.2010.07.010, 230 – 244.

Winter, G., A. van Dongeren, M. de Schipper, and J. van Thiel de Vries, 2014: Rip currents under obliquely incident wind waves and tidal longshore currents. *Coastal Engineering*, **89**, doi:https://doi.org/10.1016/j.coastaleng.2014.04.001, 106 – 119.

Wu, X., F. Feddersen, and S. N. Giddings, 2021: Characteristics and dynamics of density fronts over the inner to mid-shelf under weak wind conditions. *Journal of Physical Oceanography*, doi:10.1175/JPO-D-20-0162.1.

Wu, X., F. Feddersen, S. N. Giddings, N. Kumar, and G. Gopalakrishnan, 2020: Mechanisms of Mid- to Outer-Shelf Transport of Shoreline-Released Tracers. *Journal of Physical Oceanography*, **50**, doi:10.1175/JPO-D-19-0225.1, 1813–1837.

Figures

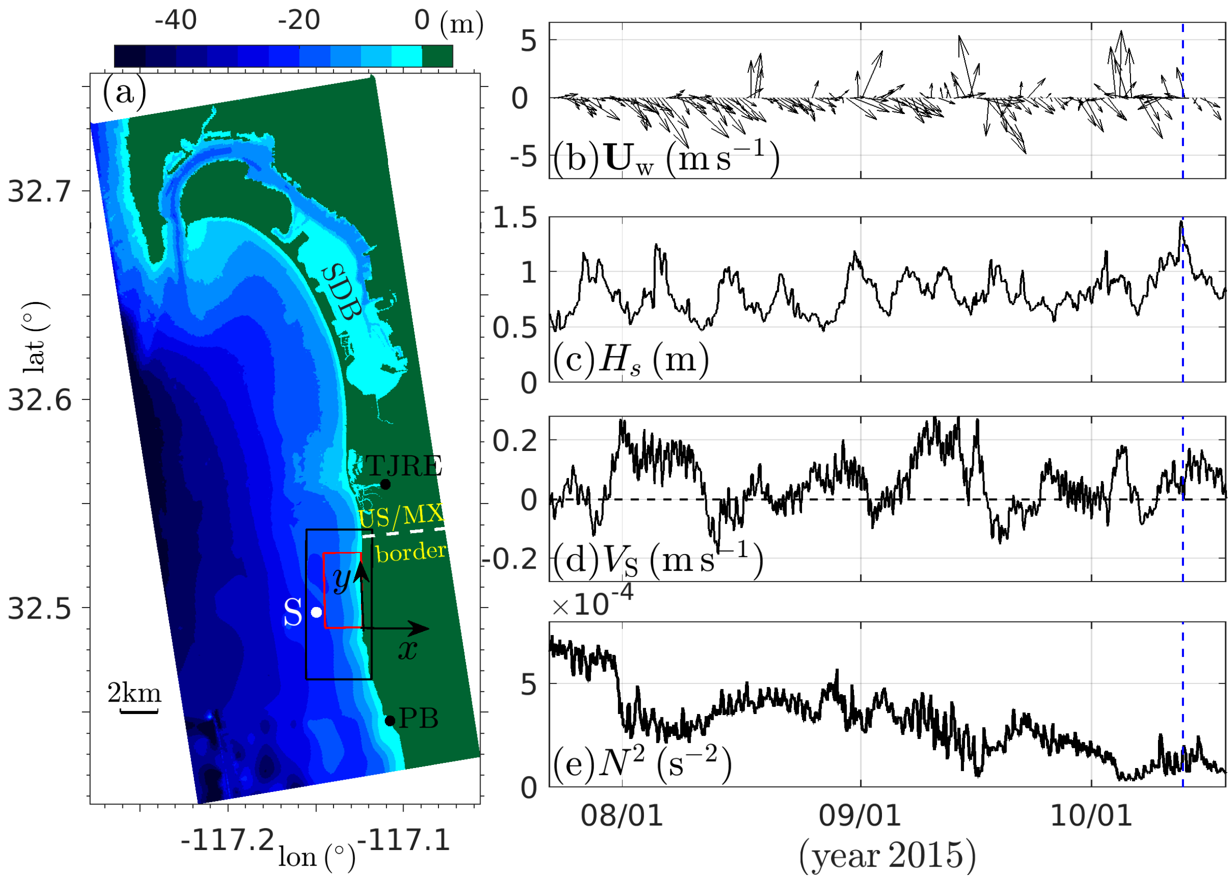

FIG. 1. (Left, a) Model grid bathymetry (color shading) map, the nearshore study region (red rectangle), and the (x, y) coordinate system aligned with east and north. The white dot denotes site S and the black rectangle denotes the zoom-in domain in Fig. 2. Black dots denote the freshwater sources Punta Bandera (PB) and Tijuana River estuary (TJRE). The San Diego Bay (SDB) and US-Mexico border are also labeled. Right: WW run time series at site S of (b) wind vector $\mathbf{U}_w$, (c) significant wave height H_s, (d) depth-averaged alongshelf current V_S (positive is northward), and (e) top-to-bottom buoyancy frequency N^2. In panels b to e, the blue dashed line corresponds to the time step in Fig. 2.

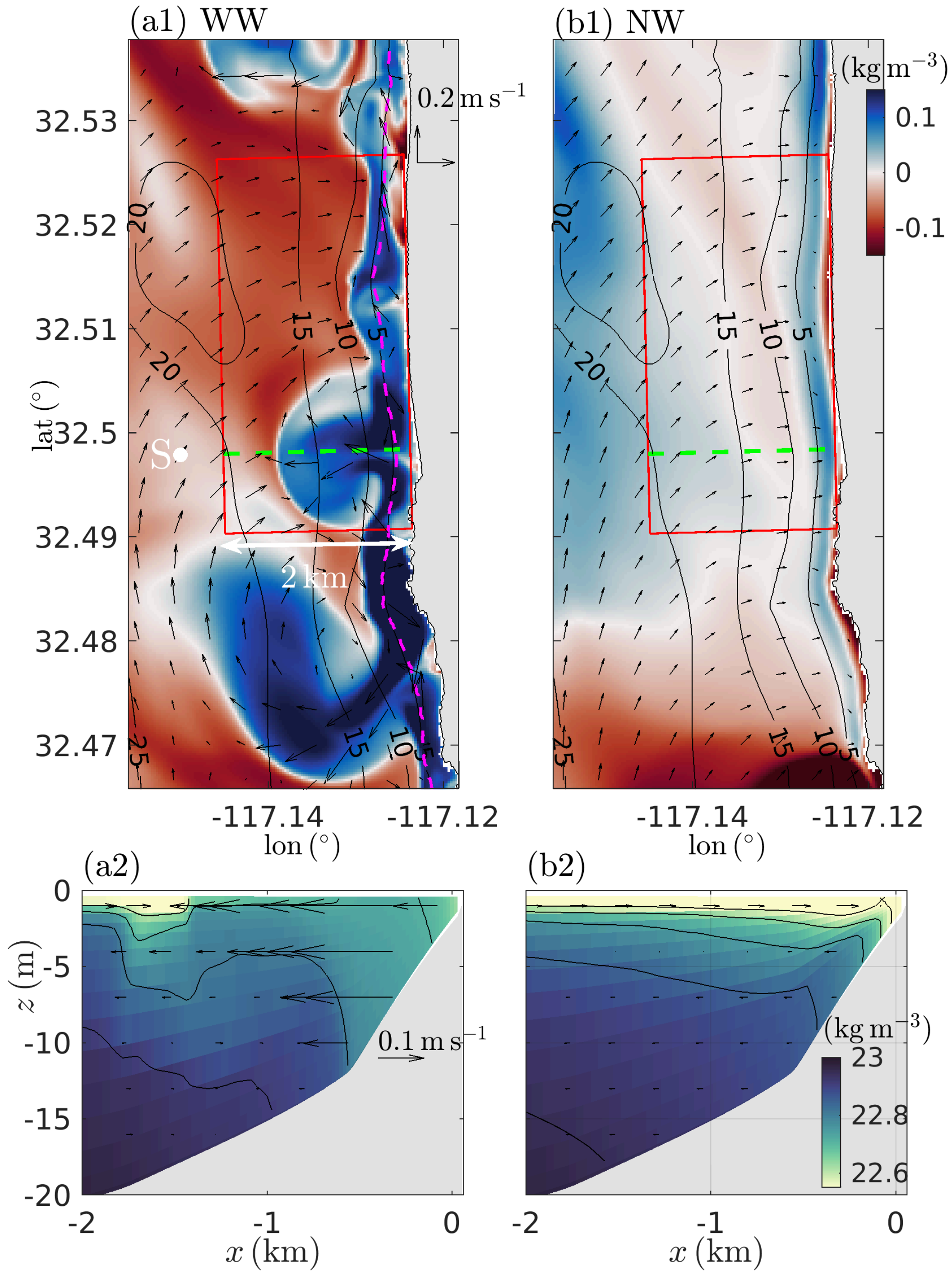

FIG. 2. (top) Snapshots of surface currents (arrows) and density anomaly (color shading, after removing the spatial mean) overlaid on bathymetry contoured at $h = [5\ 10\ 15\ 20]$ m isobaths for the (left, a1) WW and (right, b1) NW runs. The red rectangle delineates the nearshore study region. In a1, the magenta dashed line denotes the wave breakpoint location and the white dot denotes site S. (bottom) Cross-shore (x) and vertical (z) section of cross-shore currents (arrows) and density (color shading and contoured at $0.1\ \mathrm{kg\,m^{-3}}$) along the green-dashed cross-shore transect in a1 and b1 for (left) WW and (right) NW runs.

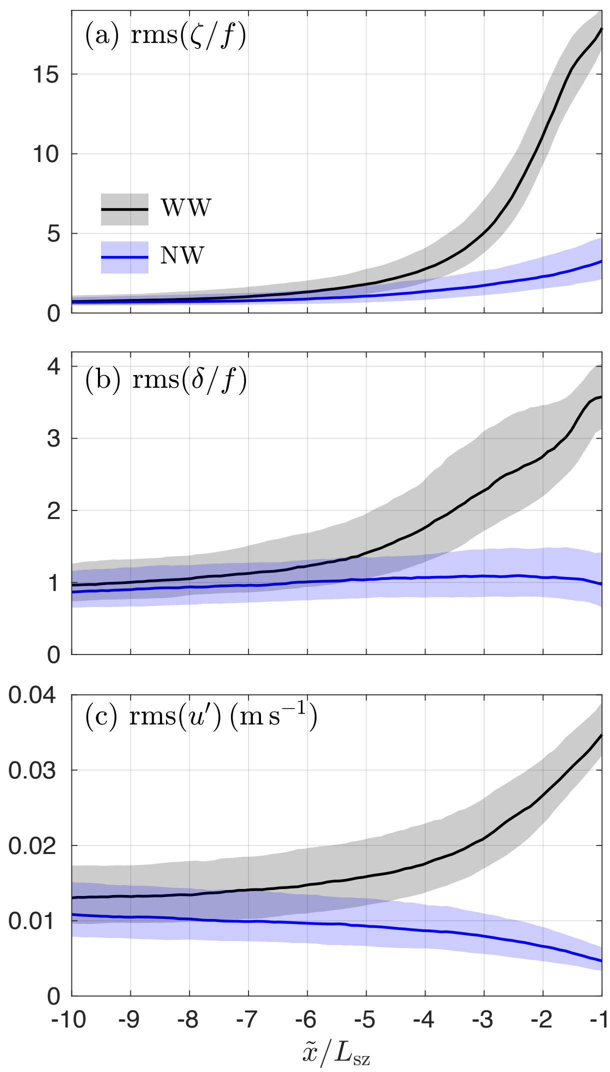

FIG. 3. The temporal median (solid) and 30%–70% (shading) of the surface alongshore root-mean-square (rms) (a) normalized vertical vorticity $\mathrm{rms}(\zeta/f)$, (b) normalized divergence $\mathrm{rms}(\delta/f)$ and (c) eddy cross-shore velocity $\mathrm{rms}(u')$ versus normalized cross-shore coordinate $\tilde{x}/L_{\mathrm{sz}}$ for the WW (black) and NW (blue) runs.

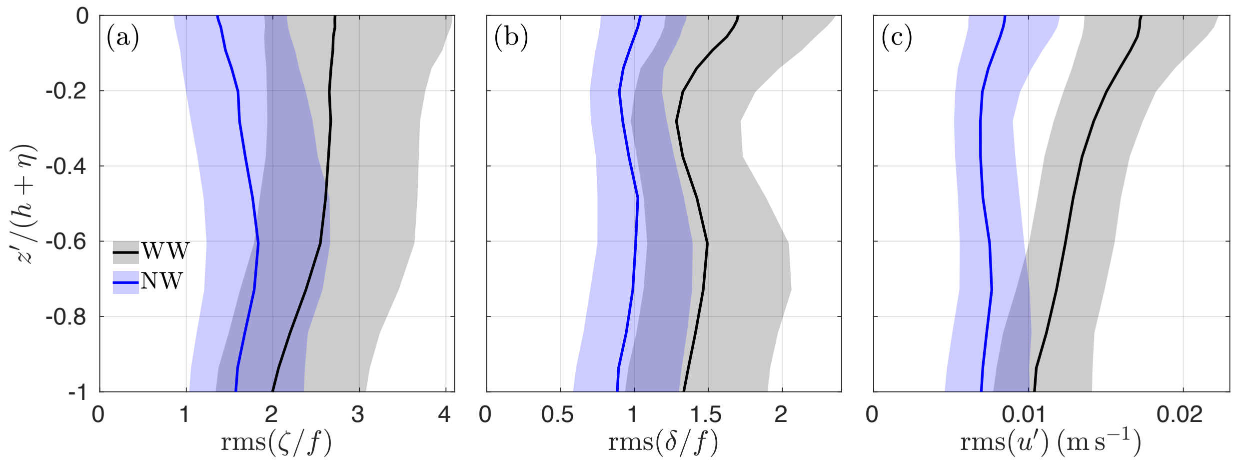

FIG. 4. The temporal median (solid) and 30%–70% (shading) of the surface alongshore root-mean-square (rms) (a) vorticity $\mathrm{rms}(\zeta/f)$, (b) divergence $\mathrm{rms}(\delta/f)$ and (c) eddy cross-shore velocity $\mathrm{rms}(u')$ versus normalized vertical coordinate $z'/(h+\eta)$ (where $z' = z - \eta$) at $\tilde{x}/L_{\mathrm{sz}} = -4$ for the WW (black) and NW (blue) runs.

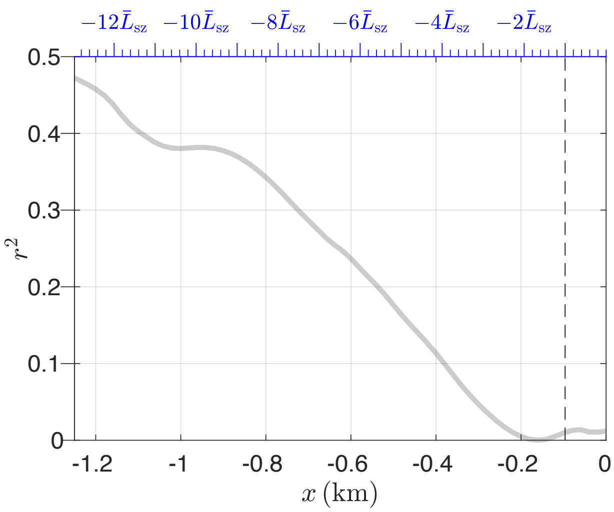

FIG. 5. Squared correlation, r^2, between the WW and NW surface eddy cross-shore velocity u' versus cross-shore distance x (on top as in time-mean surfzone width $\bar{L}_{\mathrm{sz}}$ coordinates). At each x location, r^2 is calculated over time and the alongshore.

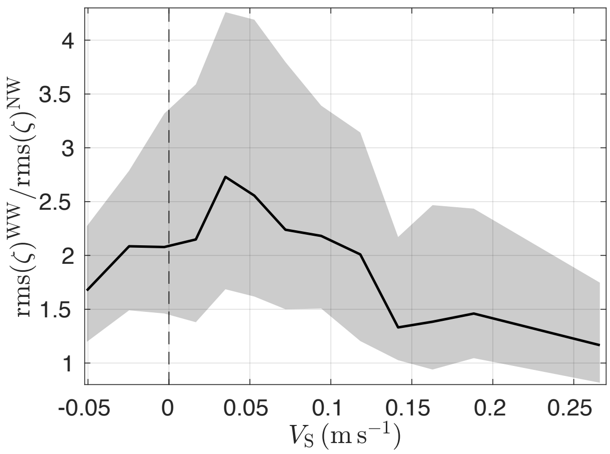

FIG. 6. The binned median (solid) and $30\% - 70\%$ (shading) of the WW to NW surface alongshore rms vorticity ratio $\mathrm{rms}(\zeta)^{(\mathrm{ww})}/\mathrm{rms}(\zeta)^{(\mathrm{nw})}$ at $\tilde{x}/L_{\mathrm{sz}} = -4$ versus the depth-averaged alongshore current at location S, V_{S}.